The Astrophysical Journal, 1005:91 (15pp), 2026 July 1 https://doi.org/10.3847/1538-4357/ae6ce5

BISTRO Survey: Gravity-dominated and Magnetically Regulated Star Formation in M17 SW

Mengke Zhao[1,2], Keping Qiu[1,2], Ji-hyun Kang[3], Xindi Tang[4], Anthony Whitworth[5], Derek Ward-Thompson[6], Takashi Onaka[7], Chang Won Lee[3,8], Tyler L. Bourke[9,10], Jihye Hwang[11,12], David Eden[13], Thiem Hoang[3,14], Motohide Tamura[7,15,16], Jungmi Kwon[7], Felix Priestley[5], Kee-Tae Kim[3,8], Doris Arzoumanian[17], James Di Francesco[18,19], Chakali Eswaraiah[20], Doug Johnstone[18,19], Bich Ngoc Nguyen[21], Zhiwei Chen[22], Sarah Sadavoy[23], Archana Soam[24], Ray S. Furuya[25], Shih-Ping Lai[26,27], Woojin Kwon[28,29], Pierre Bastien[30], Kate Pattle[31], and David Berry[32,33]

[1] School of Astronomy and Space Science, Nanjing University, 163 Xianlin Avenue, Nanjing 210023, People's Republic of China; kpqiu@nju.edu.cn
[2] Key Laboratory of Modern Astronomy and Astrophysics (Nanjing University), Ministry of Education, Nanjing 210023, People's Republic of China
[3] Korea Astronomy and Space Science Institute, 776 Daedeokdae-ro, Yuseong-gu, Daejeon 34055, Republic of Korea
[4] Xinjiang Astronomical Observatory, Chinese Academy of Sciences, 830011 Urumqi, People's Republic of China
[5] School of Physics and Astronomy, Cardiff University, The Parade, Cardiff, CF24 3AA, UK
[6] Jeremiah Horrocks Institute, University of Lancashire, Preston PR1 2HE, UK
[7] Department of Astronomy, Graduate School of Science, The University of Tokyo, 7-3-1 Hongo, Bunkyo-ku, Tokyo 113-0033, Japan
[8] University of Science and Technology, Korea (UST), 217 Gajeong-ro, Yuseong-gu, Daejeon 34113, Republic of Korea
[9] SKA Observatory, Jodrell Bank, Lower Withington, Macclesfield SK11 9FT, UK
[10] Jodrell Bank Centre for Astrophysics, School of Physics and Astronomy, University of Manchester, Oxford Road, Manchester, M13 9PL, UK
[11] Institute for Advanced Study, Kyushu University, Japan
[12] Department of Earth and Planetary Sciences, Faculty of Science, Kyushu University, Nishi-ku, Fukuoka 819-0395, Japan
[13] Armagh Observatory and Planetarium, College Hill, Armagh BT61 9DG, UK
[14] University of Science and Technology, Korea, 217 Gajeong-ro, Yuseong-gu, Daejeon 34113, Republic of Korea
[15] National Astronomical Observatory of Japan, National Institutes of Natural Sciences, Osawa, Mitaka, Tokyo 181-8588, Japan
[16] Astrobiology Center, National Institutes of Natural Sciences, 2-21-1 Osawa, Mitaka, Tokyo 181-8588, Japan
[17] Division of Science, National Astronomical Observatory of Japan, 2-21-1 Osawa, Mitaka, Tokyo 181-8588, Japan
[18] NRC Herzberg Astronomy and Astrophysics, 5071 West Saanich Road, Victoria, BC V9E 2E7, Canada
[19] Department of Physics and Astronomy, University of Victoria, Victoria, BC V8W 2Y2, Canada
[20] Department of Physical Sciences, Indian Institute of Science Education and Research (IISER) Mohali, Knowledge City, Sector 81, SAS Nagar 140306, Punjab, India
[21] Vietnam National Space Center, Vietnam Academy of Science and Technology, 18 Hoang Quoc Viet, Hanoi, Vietnam
[22] Purple Mountain Observatory, Chinese Academy of Sciences, 2 West Beijing Road, 210008 Nanjing, People's Republic of China
[23] Department for Physics, Engineering Physics and Astrophysics, Queen's University, Kingston, ON, K7L 3N6, Canada
[24] Indian Institute of Astrophysics, II Block, Koramangala, Bengaluru 560034, India
[25] Institute of Liberal Arts and Sciences Tokushima University, Minami Jousanajima-machi 1-1, Tokushima 770-8502, Japan
[26] Institute of Astronomy and Department of Physics, National Tsing Hua University, Hsinchu 30013, Taiwan
[27] Academia Sinica Institute of Astronomy and Astrophysics, No.1, Sec. 4., Roosevelt Road, Taipei 10617, Taiwan
[28] Department of Earth Science Education, Seoul National University, 1 Gwanak-ro, Gwanak-gu, Seoul 08826, Republic of Korea
[29] SNU Astronomy Research Center, Seoul National University, 1 Gwanak-ro, Gwanak-gu, Seoul 08826, Republic of Korea
[30] Centre de recherche en astrophysique du Québec & département de physique, Université de Montréal, 1375, Avenue Thérèse-Lavoie-Roux, Montréal, QC, H2V OB3, Canada
[31] Department of Physics and Astronomy, University College London, WC1E 6BT London, UK
[32] Department of Physics, University of Bath, Claverton Down, Bath, BA2 7AY, UK
[33] East Asian Observatory, 660 N. A'ohōkū Place, University Park, Hilo, HI 96720, USA
Received 2026 January 8; revised 2026 April 17; accepted 2026 May 9; published 2026 June 26

Abstract

We present high-resolution magnetic field maps of the M17 SW molecular cloud using JCMT 850 μm dust polarization at scale of 14″. The magnetic field exhibits a distinct arc-like structure that encircles three dense clumps (C1, C2, and C3). By combining polarization data with ammonia line observations, the plane-of-sky magnetic field strength, measured using the Skalidis–Tassis method to minimize angle dispersion errors, ranges from 0.1 to 2.4 mG (mean: 0.54 mG). Energy budget analysis reveals a hierarchy dominated by gravity ($e_G \approx 10^{-7.8}$ erg cm^{-3}), which exceeds both magnetic ($e_B \approx 10^{-8.3}$ erg cm^{-3}) and turbulent ($e_k \approx 10^{-8.7}$ erg cm^{-3}) energies. Since all three energy densities lie within 1 order of magnitude, gravitational dominance acts primarily as the global driver, while the system remains in a state of near equipartition. Structurally, the northeastern boundary shows magnetic field lines perpendicular to the shock front, consistent with compression from the adjacent H II region. Within the cloud, magnetic field lines generally align with gravity to assist collapse, but turn perpendicular to gravity within curved accretion bridges. This configuration provides support against radial collapse while guiding gas flow. Kinematic evidence suggests that these channels transport material from clump C3 onto the massive clump C2. Star formation in M17 SW is globally driven by gravity but locally regulated by the magnetic field structure.

Unified Astronomy Thesaurus concepts: Interstellar magnetic fields (845); Star formation (1569); Interstellar clouds (834)

1. Introduction

Star formation, a fundamental yet complex process governing interstellar medium (ISM) and galaxy evolution (F. H. Shu et al. 1987; C. F. McKee & E. C. Ostriker 2007). On galactic scales, the process is modulated by disc gravitational instabilities (A. B. Romeo & K. M. Mogotsi 2017, 2018). In contrast, the collapse of individual molecular clouds is dictated by local competition among magnetic fields (R. M. Crutcher 2012; H.-B. Li 2021; K. Pattle et al. 2023), gravity (E. Vázquez-Semadeni et al. 2019; G.-X. Li & J.-X. Zhou 2022; S. Li et al. 2024), and turbulence (R. B. Larson 1981; H.-B. Li 2021; Z. Cao & H.-b. Li 2023). However, their exact roles in the star formation process are not entirely understood (R. M. Crutcher 2012; H.-B. Li et al. 2015; K. Pattle et al. 2023). A central debate in this field concerns the relative importance of these forces: whether molecular clouds are supported by magnetic fields in a subcritical state, or whether they are governed by supercritical gravitational collapse and supersonic turbulence (R. M. Crutcher 2012; H.-B. Li 2021; K. Pattle et al. 2023). Energetically, this interplay is often quantified by comparing energy densities, such as gravitational potential energy e_G versus magnetic energy e_B (G.-X. Li & A. Burkert 2018) or dimensionless parameters like the mass-to-flux ratio (λ; R. M. Crutcher et al. 2004) and Alfvénic Mach number ($\mathcal{M}_A$; M. Zhao et al. 2024a). However, scalar metrics alone obscure the geometric (vector) role of magnetic fields. The morphology of magnetic field, gravity, and turbulence is also critical: magnetic field orientation parallel to gas flows offers little resistance to collapse, whereas fields perpendicular to the flow can provide magnetic support, channeling material into dense cores (K. Qiu et al. 2014; H.-B. Li et al. 2015; M. Zhao et al. 2024b). This distinction is particularly vital in complex environments where external feedback may reshape the cloud's geometry, potentially decoupling the local B-field orientation from the global energy budget (Y. Hu et al. 2021; M. Zhao et al. 2022).

The M17 star-forming complex, specifically the M17 SW molecular cloud (C. Lada et al. 1974; M. M. Hanson et al. 1997; M. S. Povich et al. 2009), provides an ideal laboratory to test this dual framework. Located at a distance of 1.98 kpc (Y. Xu et al. 2011; Z. Chen et al. 2012), M17 SW is a prototypical photon-dominated region (PDR) subjected to intense compressive feedback from the adjacent ionizing cluster NGC 6618 (C. J. Lada et al. 1991; M. S. Povich et al. 2009; W. Lim et al. 2020) (see Figure 1). The region features extreme column densities and active high-mass star formation, suggesting a system under strong compressive forcing. Recent studies have extensively characterized the physical environment of M17, ranging from its dust properties (Z. Chen et al. 2025) to the dense gas kinematics revealed by ammonia surveys (J. Keown et al. 2019). These works confirm the extreme nature of the region, where accurately quantifying the energy budget (scalar analysis) is essential to determining the stability of the cloud.

The magnetic field morphology of M17 has been the subject of multiwavelength investigation. On large scales, near-infrared polarimetry (Z. Chen et al. 2012) revealed a uniform magnetic field orientation aligned with the Galactic plane, suggesting that the global magnetic field is strong enough to resist turbulent randomization in the diffuse envelope. Moving to the far-infrared, observations with SOFIA/HAWC+ have traced the magnetic field into denser regions (T. D. Hoang et al. 2022). While SOFIA traces the warm dust, resolving the magnetic field geometry in dense cold structures requires the resolution and sensitivity accessible at submillimeter wavelengths.

In this work, we present 850 μm dust polarization observations of M17 SW using the James Clerk Maxwell Telescope (JCMT), as a part of B-fields In Star-forming Region Observations (BISTRO, D. Ward-Thompson et al. 2017; P. Bastien 2020). The spatial resolution in this work is significantly higher than Planck (Planck Collaboration et al. 2020) and similar to that observed by SOFIA at far-infrared (T. D. Hoang et al. 2022). Due to longer wavelengths, the dust polarization at submillimeter wavelength probes the magnetic field at the cold and inner ISM that remains optically thick in the far-infrared. Complemented by Green Bank Telescope $NH_3(1, 1)/(2, 2)$ spectroscopy (R. K. Friesen et al. 2017; J. Keown et al. 2019) tracing gas kinematics and temperature, we quantify the relative contributions of magnetic fields, gravity, and turbulence through (1) a scalar analysis using the physical parameters to establish the global energy hierarchy (e_G, e_B, e_K); and (2) a vector analysis of the alignment between magnetic fields, gravitational gradients, and velocity fields. This synthesis reveals a physical picture where gravity dictates the global collapse, while the magnetic field, shaped by external compression, regulates the specific route of mass accretion.

2. Data

2.1. Polarization Observations and Reduction

We present 850 μm dust polarization observations of M17 SW obtained with the POL-2 polarimeter on the JCMT. As part of the BISTRO survey (Project ID: M20AL018), data were acquired in the DAISY mapping mode to ensure fully sampled coverage of the target region.

The data reduction was performed using the pol2map routine within the SMURF package (D. S. Berry et al. 2005; E. L. Chapin et al. 2013) of the Starlink software suite, following the standard BISTRO data reduction pipeline (see S. Mairs et al. 2021). The raw bolometer time streams were converted into Stokes I, Q, and U maps using the iterative map-making technique `makemap`. The resulting maps were gridded to a 4″ pixel scale, sampling the 14.″1 effective beam (J. T. Dempsey et al. 2013) at 850 μm (Nyquist sampling). We applied a standard flux conversion factor (FCF) of $\sim$537 Jy pW^{-1} beam^{-1} for calibration. The total intensity (Stokes I) map is derived simultaneously with the polarization data, guaranteeing intrinsic spatial alignment.

We derived the polarization angle (θ) and fraction (p) from the Stokes parameters using the relations $\theta = 0.5\arctan(U/Q)$ and $p = PI/I$. To mitigate the positive bias in polarization measurements due to noise, we adopted the asymptotic estimator for the debiased polarized intensity (PI):

$$PI = \sqrt{Q^2 + U^2 - 0.5(\sigma_Q^2 + \sigma_U^2)}, \quad (1)$$

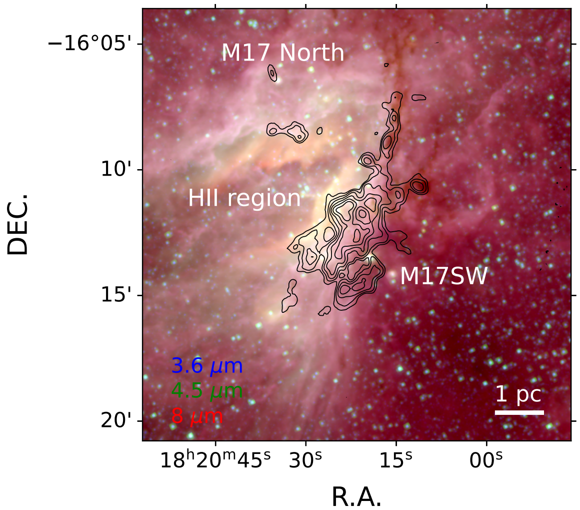

Figure 1. Large-scale mid-infrared view of the M17 star-forming complex. The background image is a three-color composite from Spitzer (R. A. Benjamin et al. 2003; S. J. Carey et al. 2009) showing the interaction between the H II region and the molecular cloud. The bright emission to the bright left/north traces the ionizing cluster NGC 6618 and the photodissociation region (PDR). The black contours show the coverage of our JCMT BISTRO 850 μm polarization observations centered on the M17 SW molecular cloud. Note the sharp boundary facing the H II region, indicative of the strong external compression discussed in the text.

where σ_Q and σ_U represent the uncertainties in Stokes Q and U, respectively. To ensure data quality for the subsequent magnetic field analysis, we selected polarization vectors based on the following criteria: $I/\sigma_I > 10$, $p/\sigma_p > 3$, and $\delta p < 5\%$, where σ_I and σ_p denote the uncertainties in total intensity and polarization fraction.

2.2. Spectral Line Data

To probe the kinematics and physical conditions of the dense gas, we utilize NH_3 (1, 1) and (2, 2) spectral line data from the *K*-band Examinations of Young Stellar Object Natal Environments (KEYSTONE) survey (Project ID: GBT15B-242; R. K. Friesen et al. 2017; J. Keown et al. 2019). Observations were carried out using the Green Bank Telescope (GBT) with the *K*-band Focal Plane Array (KFPA) and the VEGAS spectrometer.

These observations, targeting the metastable ammonia inversion transitions at 23.69–23.72 GHz, provide a velocity resolution of $\sim$0.11 km s^{-1} and a beam size of $\approx$30″. The NH_3 emission, which selectively traces dense gas ($n > 10^3$ cm^{-3}) and is less susceptible to depletion than CO, provides robust measurements of the gas systemic velocity ($v_{\rm LSR}$), velocity dispersion (σ_v), and kinetic temperature (T_K). Physical parameters were derived by fitting the hyperfine structure of the (1, 1) and (2, 2) lines simultaneously, using a forward-modeling approach as described in J. Keown et al. (2019).

3. Result

3.1. Magnetic Field Morphology

The plane-of-sky magnetic field in M17 SW is globally ordered, yet exhibits significant local deviations coincident with high-density substructures, as shown in Figure 2. Dominating the morphology is a coherent, arc-like magnetic structure encircling the central region that hosts the three dense clumps C1, C2, and C3 (see Figure 3). This magnetic arc is open toward the east, facing the ionizing cluster NGC 6618, and connects the clump C3 to the massive clumps C1 and C2. In the northwestern region, the magnetic field orientation is north–south, parallel to the local filamentary structures. In the southeastern region connecting clump C2, the magnetic field orientation reorients to an east–west direction, running perpendicular to the filamentary extended structure.

3.2. Derived Physical Parameters

To quantify the magnetic field strength and energy budget, we derived maps of the H_2 column density, volume density (ρ), characteristic scale (r), and nonthermal velocity dispersion $\sigma_{v,NT}$. The column density map (Figure 3) was calculated from the 850 μm dust continuum emission and the gas kinetic temperature derived from NH_3 hyperfine fitting (J. Keown et al. 2019; see Appendix A for details). The volume density and characteristic scale were subsequently determined using the multiscale decomposition reconstruction (MDR) method (M. Zhao et al. 2026; see Appendix B), which spatially decomposes the column density to estimate the local depth of the cloud structure assuming statistical isotropy. We isolated the nonthermal velocity dispersion from the ammonia line widths using the relation $\sigma_{v,\rm NT} = \sqrt{\sigma_{obs}^2 - k_{\rm B}T_{\rm kin}/m_{\rm NH3}}$, where σ_{obs} is the observed velocity dispersion and $m_{\rm NH3}$ is the molecular mass of ammonia. Unlike diffuse tracers (e.g., ^{12}CO and ^{13}CO) that require statistical filtering to mitigate extended line-of-sight (LOS) contamination (A. Polychronakis et al. 2025), NH_3 preferentially traces high-density material. This inherently isolates the core dynamics from large-scale flows that could otherwise bias our results (F. D. Priestley & A. P. Whitworth 2021). Hereafter, $\sigma_{v,NT}$ is adopted as the tracer of turbulence along the LOS for all energy density and magnetic field strength calculations.

To quantify the gravitational energy, we calculated the gravitational potential (Φ) directly from the column density map. Following the 2D gravitational potential measurement (Z.-Z. He et al. 2023), we solved the Poisson equation in Fourier space assuming a simplified geometry appropriate for the projected data:

$$\Phi_k = -\frac{2\pi G\Sigma_k}{|\boldsymbol{k}|(1 + |\boldsymbol{k}|H_{\rm eff})}, \quad (2)$$

where Σ_k is the Fourier transform of the mass surface density ($\Sigma = \mu m_H N_{\rm H_2}$), $\boldsymbol{k}$ is the wavevector, and $H_{\rm eff}$ represents an effective half-thickness (0.3 pc, see Figure 12). This approach allows us to recover the 3D potential structure from the projected mass distribution, which is then used to compute the gravitational energy density $e_G = \Phi\rho$ in Section 3.4 and direction of gravitational acceleration $a_G = \nabla\,\Phi$ (detail in Section 4.2.2).

3.3. Magnetic Field Strength

We estimate the plane-of-sky magnetic field strength ($B_{\rm pos}$) using the Skalidis–Tassis (ST) method (R. Skalidis & K. Tassis 2021), according to the energy equipartition between turbulence and magnetic field of the compressibility of turbulence in molecular clouds. The field

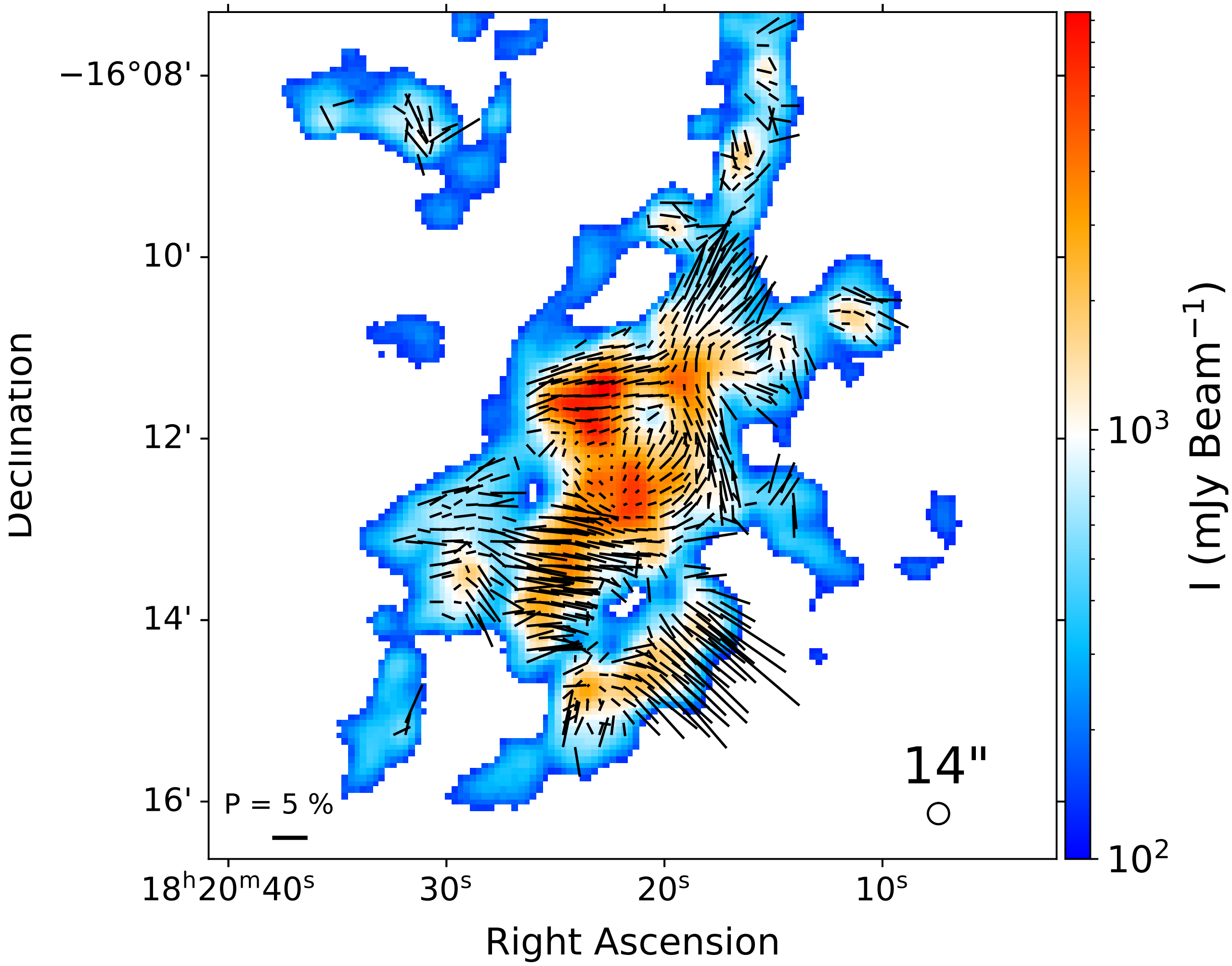

Figure 2. Magnetic field morphology of M17 SW from 850 μm dust polarization. The background presents the dust continuum emission at 850 μm. The black lines show the magnetic field orientations, and their lengths are proportional to the polarization fraction (p).

strength is calculated as

$$B_{\rm pos} = \sqrt{2\pi\rho}\frac{\sigma_{v,NT}}{\sqrt{\sigma_\theta}}, \tag{3}$$

where ρ is the volume density, $\sigma_{v,{\rm NT}}$ is the nonthermal velocity dispersion derived from NH_3 line width, and σ_θ is the angular dispersion of the magnetic field (see Appendix C for details).

To calculate σ_θ, we separated the ordered large-scale magnetic field as background field from the turbulent component by convolving the Stokes Q and U maps with a Gaussian kernel having a FWHM of 42″, corresponding to approximately 3× the beam size:

$$\sigma_\theta = \sqrt{\frac{1}{N}\sum(\theta_i - \bar{\theta})^2}. \tag{4}$$

We excluded pixels with $\sigma_\theta > 25°$ where the dispersion analysis becomes unreliable. To ensure physical consistency, all input parameter maps (ρ, $\sigma_{v,NT}$) were smoothed to the same 42″ resolution used for the dispersion analysis (see Figure 13).

Figure 4 presents the spatial distribution and statistics of the plane-of-sky magnetic field strength ($B_{\rm pos}$). The magnetic field strength ranges from 0.1 to 2.4 mG, with a mean value of ∼0.54 mG. The highest magnetic field strengths are spatially correlated with the dense clumps C1 and C2. To verify the robustness of these estimates, we also performed a calculation using the classical Davis–Chandrasekhar–Fermi (DCF) method. As detailed in Appendix D, the DCF method yields a consistent mean magnetic field strength (∼0.69 mG), confirming the high magnetization of the region regardless of the specific method employed.

3.4. Energy Density Distribution

To compare the magnetic field, turbulence, and gravity within a consistent physical framework (same dimension), we assess the dynamical state of M17 SW by comparing the energy densities of the three dominant mechanisms: gravitational potential energy ($e_G = \Phi\rho$), magnetic energy ($e_B = B_{\rm tot}^2/8\pi$), and turbulent kinetic energy ($e_k = \frac{1}{2}\rho\sigma_{v,{\rm 3D}}^2$).

To ensure dimensional consistency in the energy budget, the total magnetic field strength is estimated by the projected factor ($B_{\rm tot} \approx \frac{4}{\pi}B_{\rm pos}$; R. M. Crutcher et al. 2004). As a consistency check, if we decompose this derived $B_{\rm tot}$ assuming random orientation, the implied LOS component is approximately ∼0.4 mG. This matches the magnitude of $B_{\rm los}$ directly measured via H I Zeeman splitting in the M17 envelope (-450/+550 μG; C. L. Brogan et al. 1999). This consistency supports the validity of using the statistically corrected field strength for our dynamical analysis.

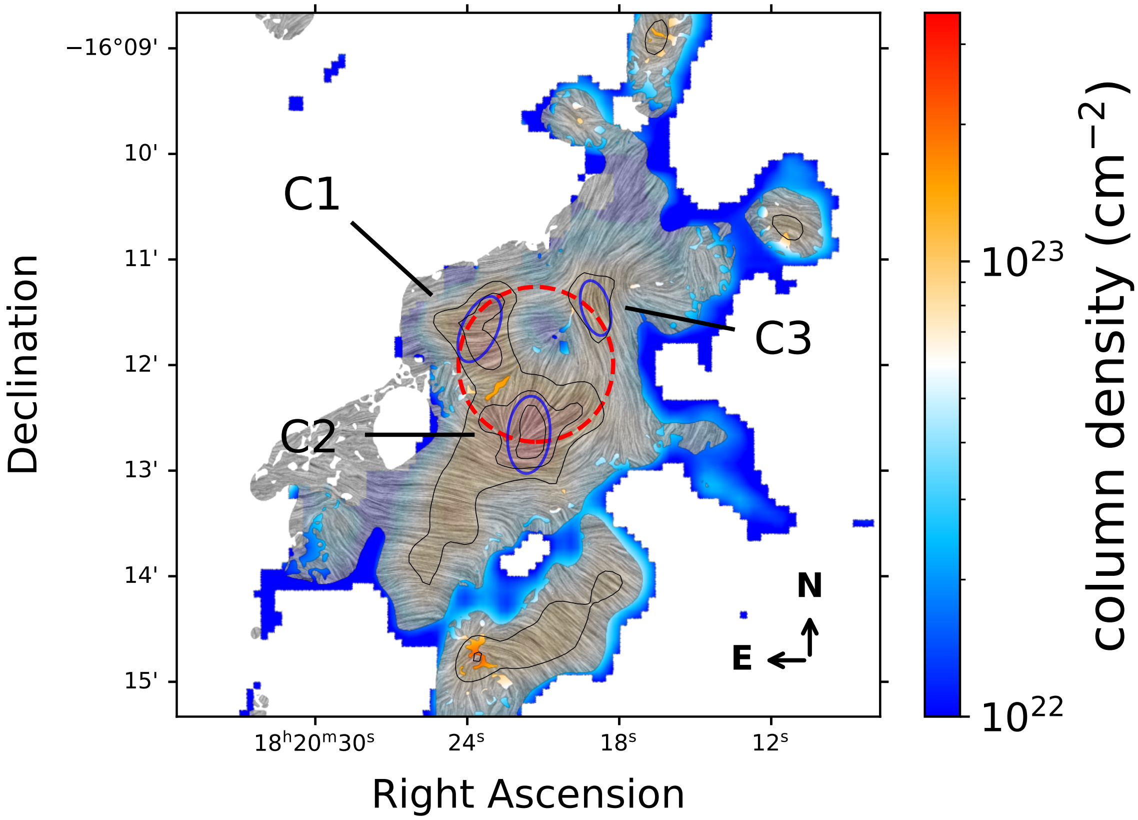

Figure 3. Magnetic field morphology and density structure. The line integral convolution map presents the magnetic field morphology from BISTRO dust polarization at scale of 14″. The background shows the H_2 column density at a scale of 30″ and the black contours display the column density as 1, 2, 3 × 10^{23} cm^{-2}, respectively. The three blue ellipses show the three dense clumps classified by column density structure and located in a circular shape.

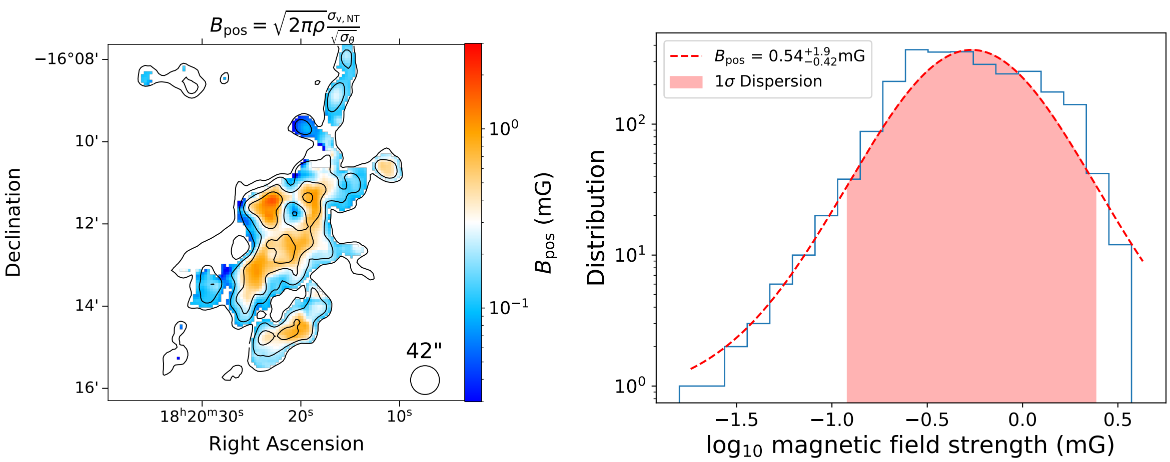

Figure 4. Projected magnetic field strength distribution derived using the Skalidis–Tassis (ST) method. Left panel: spatial distribution of the plane-of-sky magnetic field strength (B_{pos}) across the M17 SW cloud. Black contours show the 850 μm emission from $10^{2.5}$ to 10^4 mJy $beam^{-1}$. Right panel: probability density function (pdf) of the magnetic field strength (B_{pos}) at POS. The red dashed line represents a Gaussian fit to the distribution. The shaded pink region corresponds to the 1σ dispersion range, highlighting the spatial variation of the magnetic field strength. The legend indicates the mean value and the asymmetric dispersion limits derived from the fit. All calculations are performed on maps smoothed to a common resolution of 42″ to ensure consistency between the polarization and spectroscopic data.

Figure 5 (left panel) displays the composite spatial distribution of these energy densities. Gravitational energy (e_G) is most concentrated within the dense cores C1–C3, while magnetic energy (e_B) appears widespread, showing enhancement along the arc-like structure facing the H II region. The probability density functions (pdfs) of the energy densities (Figure 5, right panel) are well described by log-normal distributions. The derived mean values are $\langle \log e_G \rangle \approx -7.84$, $\langle \log e_B \rangle \approx -8.25$, and $\langle \log e_k \rangle \approx -8.71$ (in units of erg cm^{-3}).

While the mean values suggest a hierarchy of $e_G \gtrsim e_B \gtrsim e_k$, the energy density pdfs exhibit overlap, as shown by the 1σ dispersion widths in Figure 5. The differences between the mean energy densities are generally within 1 order of magnitude (and often within the factor of ∼2–3 uncertainty typical of these estimates). This indicates that M17 SW is not

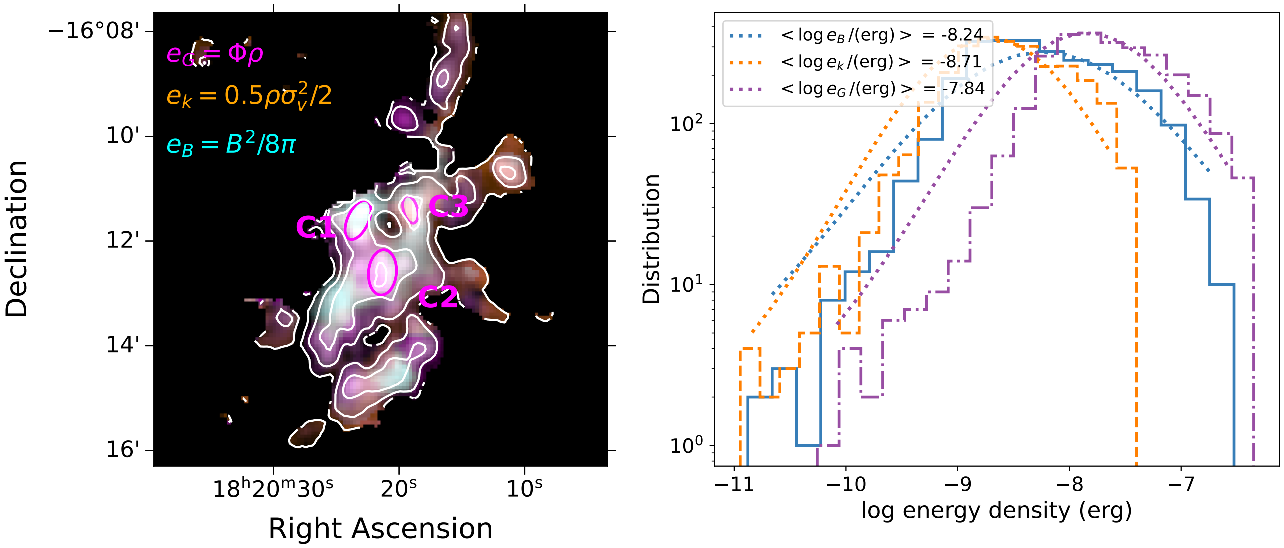

Figure 5. Comparison of gravitational, magnetic, and turbulent energy densities in M17 SW. Left panel: composite RGB map displaying the spatial distribution of energy densities. Purple represents the magnitude of gravitational potential energy density ($|e_G| = \Phi\rho$), orange shows turbulent kinetic energy density ($e_k = 0.5\rho\sigma_v^2$), and cyan indicates magnetic energy density ($e_B = B^2/8\pi$). The magnetic energy density e_B is estimated by applying a statistical correction ($B_{tot} \approx 4/\pi B_{\rm pos}$) to the POS magnetic field strength. The background is masked to show only the region with column density measurements ($N_{\rm H_2} > 10^{22}$ cm^{-2}). The red ellipses mark the positions of the dense clumps C1, C2, and C3. Right panel: probability density functions (pdfs) of the three energy components. The dashed lines represent Gaussian fits to the distributions, with the mean values indicated in the legend. This overlap suggests that while gravitational energy is marginally dominant (highest mean), the system is globally in a state of near equipartition, necessitating a vector analysis to understand the collapse dynamics. All energy densities are calculated in cgs units (erg cm^{-3}) and are based on maps smoothed to a common resolution of 42″.

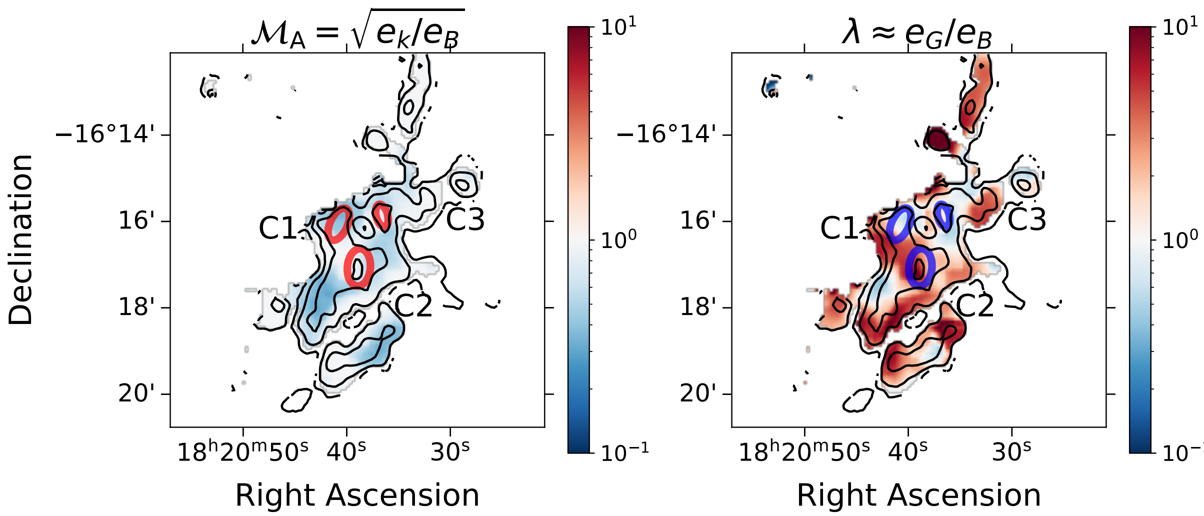

Figure 6. Distribution of Alfvénic Mach number and mass-to-flux ratio. The backgrounds display the distribution of $\mathcal{M}_{\rm A}$ and λ. The contours show the structure of column density.

dominated solely by gravity but is rather in a state of global near equipartition, where magnetic fields and turbulence remain dynamically significant competitors to gravitational collapse.

To facilitate comparisons with other star-forming regions (e.g., K. Pattle et al. 2017, 2023), we recast the energy density analysis into two standard dimensionless parameters: the Alfvénic Mach number ($\mathcal{M}_{\rm A}$) and the normalized mass-to-flux ratio (λ). The Alfvénic Mach number, representing the ratio of turbulent to magnetic energy, is estimated as

$$\mathcal{M}_{\rm A} = \frac{\sigma_v}{v_{\rm A}} = \frac{\sigma_v}{B_{\rm tot}/\sqrt{4\pi\rho}} = \sqrt{\frac{(1/2)\rho\sigma_v^2}{B_{\rm tot}^2/8\pi}} \equiv \sqrt{\frac{e_k}{e_B}}. \quad (5)$$

Similarly, adopting a flattened geometry, the mass-to-flux ratio approximates the balance between gravity and magnetic fields as

$$\lambda = \frac{(M/\Phi){\rm obs}}{(M/\Phi){\rm crit}} = \frac{\Sigma \cdot A/(B_{\rm tot} \cdot A)}{1/(2\pi\sqrt{G})} = 2\pi\sqrt{G}\frac{\Sigma}{B_{\rm tot}} \approx \sqrt{\frac{e_G}{e_B}}. \quad (6)$$

Figure 6 presents the spatial distribution of $\mathcal{M}_{\rm A}$ and λ derived from the energy density maps. The cloud exhibits a mean $\mathcal{M}_{\rm A} \approx 0.6$, placing it in a trans- to sub-Alfvénic regime where magnetic tension effectively regulates turbulence. However, with a mean $\lambda \approx$ 2–3, the region remains magnetically supercritical, indicating that magnetic support is globally

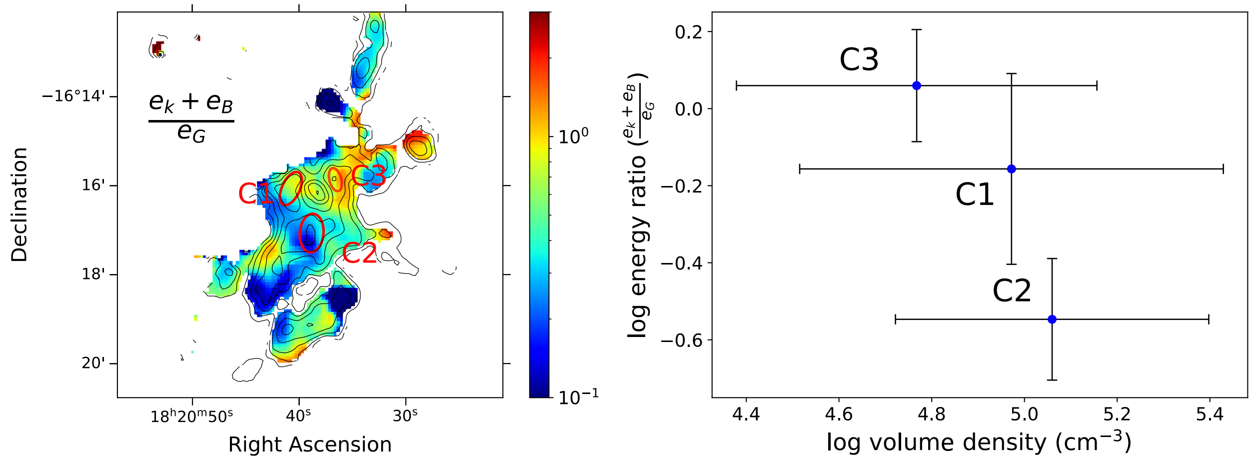

Figure 7. Energy ratio between turbulence, magnetic field, and gravity in M17 SW. The left panel shows the energy ratio $((e_B + e_k)/e_G$ in M17 SW. The black contours present the column density structure from 1×10^{22} to $3 \times 10^{23.3}$ cm^{-2} with the step of 0.3 dex. The right panel shows the distribution of clumps C1, C2, and C3 in the volume density-energy ratio plane. The error bars of clumps present their distribution in the volume density-energy ratio plane.

insufficient to halt the gravitational collapse driven by the dominant potential energy.

4. Discussion

4.1. Scalar Analysis: Global Near Equipartition and Supercriticality

The energy density analysis (Section 3.4) presents a dynamical state defined by competition rather than absolute dominance. While the mean gravitational potential energy density ($\langle \log e_G \rangle \approx -7.84$) exceeds the magnetic ($\langle \log e_B \rangle \approx -8.25$) and turbulent ($\langle \log e_k \rangle \approx -8.71$) components, the pdfs exhibit significant overlap (see Figure 5). This implies that M17 SW is globally in a state of near equipartition, where neither magnetic fields nor turbulence can be neglected.

Figure 7 maps the spatial variation of this energy balance. The ratio $(e_k + e_B)/e_G$ exhibits a clear bimodality: the central dense clumps C1 and C2 are characterized by low ratios (<1), consistent with localized gravitational collapse. In contrast, the envelope regions—particularly the arc facing the H II region—show ratios approaching or exceeding unity, indicative of magnetic or turbulent support against gravity.

The dimensionless parameters derived in Section 3.4 reinforce this picture. The prevalence of magnetically supercritical yet sub-Alfvénic conditions confirms that while magnetic tension cannot halt the global gravitational collapse, it is sufficiently strong to suppress turbulent disruption. Furthermore, since plane of sky measurements underestimate the mass-to-flux ratio (A. Tritsis 2026), our derived supercriticality represents a lower limit. Synthesizing these scalar diagnostics, M17 SW emerges as an unstable system driven by gravity, where the collapse is likely retarded rather than freefall. This suggests a mode of star formation that is globally gravity dominated but locally regulated by a strong, ordered magnetic field. To decipher the mechanics of this regulation, we now turn to a vector analysis of the magnetic field geometry.

4.2. Vector Analysis: The Squeeze-and-channel Mechanism

Vector analysis of magnetic fields, gravity, and gas flows is crucial to reveal the dynamics of physical processes, where scalar analysis only studies the energy budget. The observed

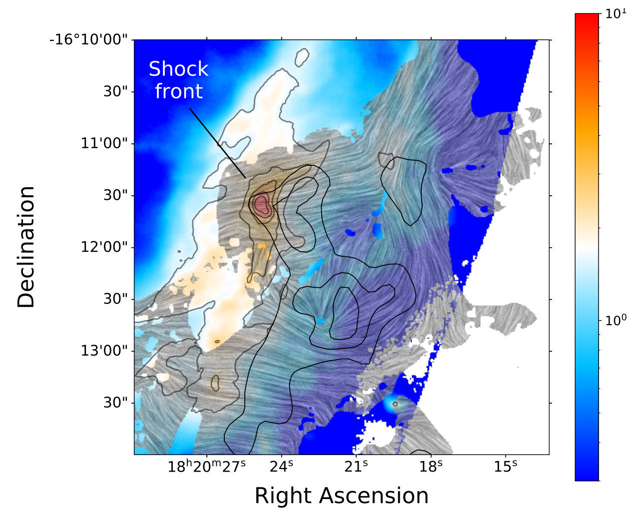

Figure 8. Observational signature of external compression. The background image shows 37 μm emission tracing the warm dust of the PDR and shock front. The overlaid streamlines depict the magnetic field morphology derived from BISTRO data. The magnetic field exhibits a prominent perpendicular alignment to the shock front along the northeastern boundary.The magnetic field exhibits a perpendicular alignment to the shock front along the northeastern boundary.

morphology supports a "squeeze-and-channel" mechanism, resulting from the interaction between magnetic field and external feedback, and gravity.

4.2.1. External Squeezing: Shock-driven Alignment

Figure 8 shows the magnetic field along the northeastern boundary, adjacent to clumps C1 and C2. This region coincides with the PDR shock front traced by 37 μm warm dust emission (W. Lim et al. 2020). Along this shock interface and the extended structure southeast of C2, the magnetic field is perpendicular to the shock front.

This perpendicular alignment is consistent with strong external compression (or potentially cloud–cloud collision; F.-Y. Zhu et al. 2023) driven by the expanding H II region. The shock from the H II region hits the molecular cloud and drags the magnetic field lines along the direction of shock propagation (Y. Hu et al. 2019; M. Zhao et al. 2024a). This

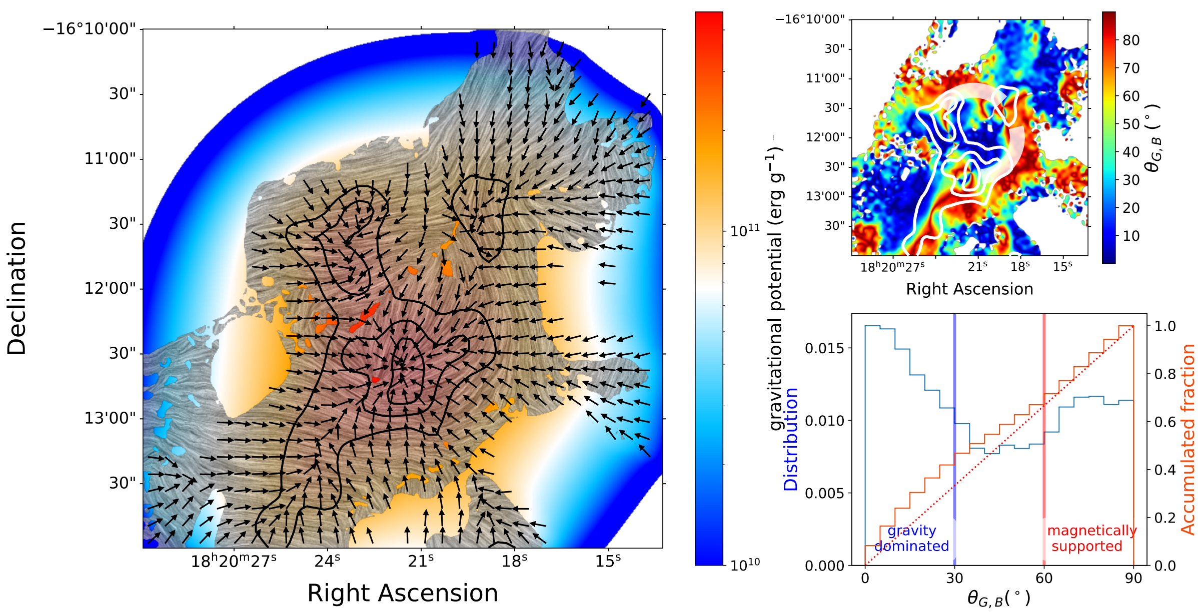

Figure 9. Alignment between gravity and magnetic field in M17 SW. Left panel: gravitational potential overlaid with magnetic field vectors. The LIC map shows the magnetic field orientation, and the black arrows present the direction of local gravity. The background is the gravitational potential at POS. Top-right panel: spatial distribution of the alignment angle $\theta_{G,B}$. The white dashed paths highlight the "magnetic bridges" connecting C3 to C1/C2. The bridge regions clearly exhibit perpendicular alignment ($\theta_{G,B} \approx 90°$, red/yellow), indicating localized magnetic support against radial collapse. Bottom-right panel: statistical distribution of alignment angles. The blue line shows the distribution offset angle between magnetic field and gravity. The red line presents the accumulation fraction of offset angle, and the dotted line is the random distribution of the accumulation fraction. The shaded blue region ($\theta_{G,B} < 30°$) represents the gravity-dominated regime that governs the global cloud, while the red region ($\theta_{G,B} > 60°$) corresponds to the magnetically supported regime found within the accretion bridges.

indicates that the external H II region shapes the cloud envelope through shock compression (T. L. Wilson et al. 2003; T. J. Haworth et al. 2015; F.-Y. Zhu et al. 2023).

4.2.2. Accretion Bridges: Magnetically Regulated Gas and Support Against Gravity

The magnetic fields form two curved structures connecting clump C3 to the massive clumps C1 and C2, respectively (see Figure 3). Clump C2 acts as the gravitational center of the region, characterized by the lowest energy ratio and strongest gravitational dominance (see Figure 7). While these curved structures are faint in the column density map, they are clearly defined in the offset angle map (Figure 9) by their specific alignment: the magnetic field is perpendicular to the local gravity gradient ($\theta_{G,B} \approx 90°$). We identify these structures as "accretion bridges," where the magnetic field channels gas flow.

These accretion bridges create a selective support mechanism. Across the bridge, magnetic pressure resists gravity, preventing radial collapse and maintaining the channel shape. Parallel to the bridge axis, however, magnetic resistance is minimal. We estimate the enclosed mass of the dense clumps C1 and C2 to be a few $\times 10^3 M_\odot$ based on the column density integration. A simple dynamic estimate (assuming gravitational acceleration from rest) suggests that this local mass alone might be marginally insufficient to accelerate gas from rest to the observed velocities over the length of the bridge ($\sim$1 pc). However, the accretion flow is likely driven by the global gravitational potential of the entire M17 SW cloud (total mass $>10^4 M_\odot$, derived from column density; see Figure 11), rather than by the local clumps alone. As gravity is a long-range force, the massive envelope contributes significantly to the acceleration. Furthermore, the gas likely enters these magnetic channels with nonzero initial momentum derived from the external shock compression (H II region expansion). The moderate local mass (mass of clumps C1 and C2 $\sim 3 \times 10^3 M_\odot$) is actually critical for this regulation; if the local mass were higher ($>10^4 M_\odot$), the local gravitational energy would likely overwhelm the magnetic support, disrupting the bridge geometry and leading to freefall collapse.

This mechanism allows gas to move toward the gravity center. We extracted a position–velocity (PV) diagram along the spatial spine of the accretion bridges connecting C1, C3, and C2. As shown in the bottom panel of Figure 10, the NH_3 emission exhibits a continuous and coherent velocity gradient of $\sim$4–6 km s^{-1} pc^{-1} along these specific tracks. Driven by the strong gravity of C2 (and the global potential, see Figure 9), gas flows unimpeded from C3 through magnetically supported bridges (see Figure 7). The magnetic field acts as a structural guide, channeling this shock-injected, gravity-assisted flow directly onto the potential well of C2, preventing the gas from dispersing or stalling.

4.3. Synthesis: A Unified Physical Picture

Combining the energy budget (scalar) and alignment (vector) analyses, we propose a physical scenario for M17 SW, characterized as a squeeze-and-channel process:

1. *External compression.* The interaction begins at the northeastern boundary. The expanding H II region (NGC 6618) drives a strong shock into the molecular cloud. This event, likely a cloud–cloud collision, compresses the gas and drags the magnetic field lines, aligning them perpendicular to the shock front. This external force defines the high-density envelope of the cloud.
2. *Magnetic channeling in accretion flows.* Distinct from the shock front, the magnetic field organizes into curved accretion bridges connecting the gas reservoir (C3) to the

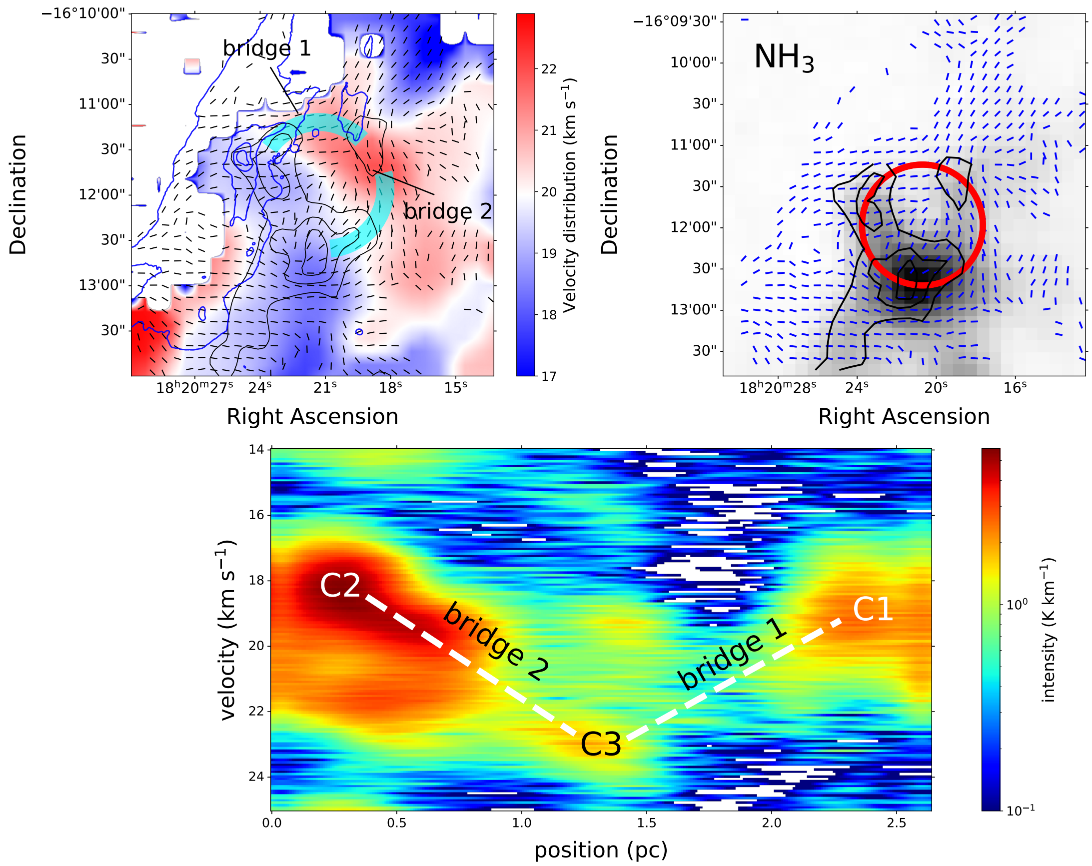

Figure 10. Kinematic signatures of the accretion bridges. Top left: line-of-sight (LOS) velocity field derived from NH_3 (color background) overlaid with the magnetic field morphology (black lines) and column density contours (black, starting from 1×10^{23} to 3×10^{23} cm^{-2} in steps of 1×10^{23} cm^{-2}). The cyan curves outline the spatial trajectories of the two accretion bridges. Top right: NH_3 integrated intensity map. The red circle highlights the central gravitational hub region encompassing the clumps. Bottom: position–velocity (PV) diagram extracted along the spine of the accretion bridges (from C1 through C3 to C2, matching the white dashed track). This PV diagram presents the velocity gradients characterizing the magnetically channeled gravitational accretion. The white dotted lines show the accretion bridge between C3 and C1, C2 (see Figure 3).

gravitational center (C2). These accretion bridges provide selective support: magnetic pressure prevents the gas from collapsing radially, maintaining the bridge structure, while allowing free movement along the bridge axis.

3. *Gravitational drive.* Although the system is near energy equipartition, gravity remains the primary driver. It pulls gas from C3 through these magnetically supported bridges, accumulating mass onto the massive clump C2.

In summary, star formation in M17 SW is globally driven by gravity but locally regulated by magnetic fields. The external shock shapes the initial condition, the magnetic field defines the accretion pathways, and gravity powers the final mass accumulation.

5. Summary

In this work, we study the roles of magnetic fields, gravity, and turbulence in the massive star-forming region M17 SW by energy density analysis and kinetic analysis, combining high-resolution 850 μm dust polarization observations (BISTRO/JCMT) with NH_3 spectral line data. Our main findings are as follows:

1. *Magnetic field morphology and strength.* The magnetic field exhibits a striking ringlike structure surrounding the three massive clumps (C1, C2, C3). The POS magnetic field strength, measured using the ST method, ranges from 0.1 to 2.9 mG, with a mean strength of 0.54 mG.

2. *Energy budget and near-equipartition system.* Analysis of the energy densities reveals a clear hierarchy: gravity dominates ($\langle e_G \rangle \approx 10^{-7.84}$ erg cm^{-3}), followed by magnetic energy ($\langle e_B \rangle \approx 10^{-8.25}$ erg cm^{-3}), and then turbulent energy ($\langle e_k \rangle \approx 10^{-8.71}$ erg cm^{-3}). The cloud is magnetically supercritical ($\lambda \gtrsim 1$) and sub-Alfvénic state ($\mathcal{M}_A \lesssim 1$), where the gravity dominates the main physical process and the magnetic field also plays an important role. Due to the energy densities of gravity, magnetic field, and turbulence on 1 order of magnitude, the M17 SW could be close to a near-energy-equipartition system.

3. *Accretion bridges and channeling flow.* We identified curved "accretion bridges" connecting clump C3 to the massive clump C2. In these bridges, the magnetic field is perpendicular to gravity. This configuration provides support against radial collapse but allows gas to flow freely along the bridge axis. Velocity gradients confirm that gas is flowing from C3 onto C2. This flow is likely powered by the global gravitational potential and guided by the magnetic field lines.

4. *External shock.* The northeastern boundary shows signs of strong external compression from the adjacent H II region. Here, the magnetic field is perpendicular to the shock front, consistent with magnetic field lines being dragged by a shock. This external force defines the dense envelope of the cloud.

Star formation in M17 SW is globally driven by gravity but locally regulated by the magnetic field. The external shock shapes the cloud's initial structure, the magnetic field defines the accretion channels, and gravity powers the final accumulation of mass onto the cores.

Acknowledgments

M.Z. acknowledges support from the National Natural Science Foundation of China (NSFC) grant No. 12503029. K. Q. is supported by NSFC grant No. 12425304, the National Key R&D Program of China (Nos. 2023YFA1608204 and 2022YFA1603103), and the grant from the China Manned Space Project. E.C. acknowledges the support from Core Research Grant (CRG; sanction order number CRG/2023/008710) awarded by Anusandhan National Research Foundation (ANRF) under Science and Engineering Research Board (SERB), Govt. of India.

Appendix A
Column Density

The column density is a fundamental physical parameter to describe the mass distribution of the ISM on the plane of sky. In general, it can be calculated by the blackbody model and the intensity of the continuum. In this work, we use the intensity map of 850 μm emission, observed by JCMT Scuba-2, to measure the column density map. According to the blackbody function, the column density traced by warm and cold dust can be calculated as

$$\Sigma = \frac{RS_\nu}{B_\nu(T_{\rm dust})\kappa_\nu}, \quad \text{(A1)}$$

where R is the gas-to-dust mass ratio (≈100), S_ν is monochromatic flux at frequency ν, $B_\nu(T_{\rm dust})$ is the Planck function at the dust temperature $T_{\rm dust}$, and κ_ν is the dust opacity (≈1.48 $\mathrm{cm^2\,g^{-1}}$ at 850 μm, based on the Mathis—Rumpl—Nordsieck (1977) model with thin ice mantles after 10^5 yr; V. Ossenkopf & T. Henning 1994). The dust temperature is similar to the temperature of dense molecular gas, probed by NH_3 from GBT (R. K. Friesen et al. 2017), which assumes similar temperatures of gas and dust. To uniform the spatial resolution, the 850 μm emission is smoothed as 30″, the same resolution as NH_3. Then, using Equation A1, the column density is calculated at the scale of 30″ (see Figure 11).

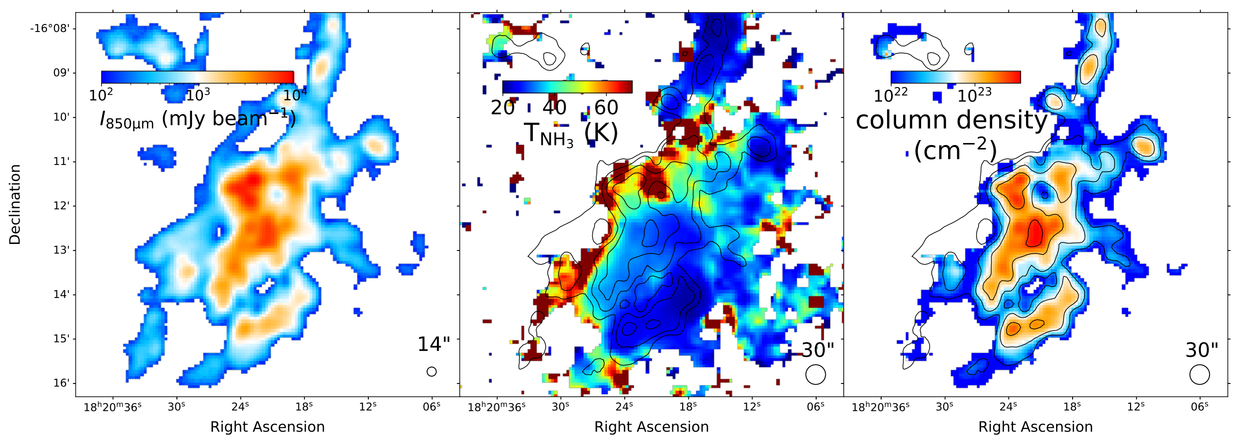

Figure 11. Distribution of column density is measured by 850 μm emission and dense gas temperature (NH_3). The panels present the distribution of 850 μm emission, gas temperature from NH_3 (R. K. Friesen et al. 2017), and H_2 column density, from left to right.

Appendix B
Mapping Volume Density and Characteristic Scale

In this work, we derive the volume density (ρ) and characteristic scale (l_c) distributions using the MDR method (M. Zhao et al. 2026), which is built upon the constrained diffusion algorithm (G.-X. Li 2022).

Traditional density estimations assume a uniform LOS thickness across the entire cloud. Such a rigid assumption overestimates volume densities in extended diffuse envelopes and underestimates them in compact dense cores. The MDR method overcomes this structural bias by dynamically extracting the local structural width from the column density map (M. Zhao et al. 2026).

The MDR method operates by (1) decomposing the column density map into scale-dependent components; (2) computing the intensity-weighted characteristic scale (l_c) at each position; and (3) deriving the volume density under the assumption of local statistical isotropy. Here, the LOS effective thickness is locally approximated by the POS structural width ($l_{\rm t,LOS} \approx l_c$), allowing the thickness to adapt to the hierarchical structure of the cloud (E. Vázquez-Semadeni et al. 2019). Figure 12 presents the resulting POS distributions of the volume density and characteristic scale in M17 SW.

While macroscopic external compression (e.g., from the adjacent H II region at the northeastern boundary) might introduce local geometric flattening, this variable-thickness framework is fundamentally superior to a constant-thickness assumption. M. Zhao et al. (2026), using the 3D MHD validation, demonstrate that this statistically isotropic scaling inherently captures the core-envelope density contrast and robustly constrains the global density uncertainties within a factor of ~2, fulfilling the requirements for dynamical analyses in this work.

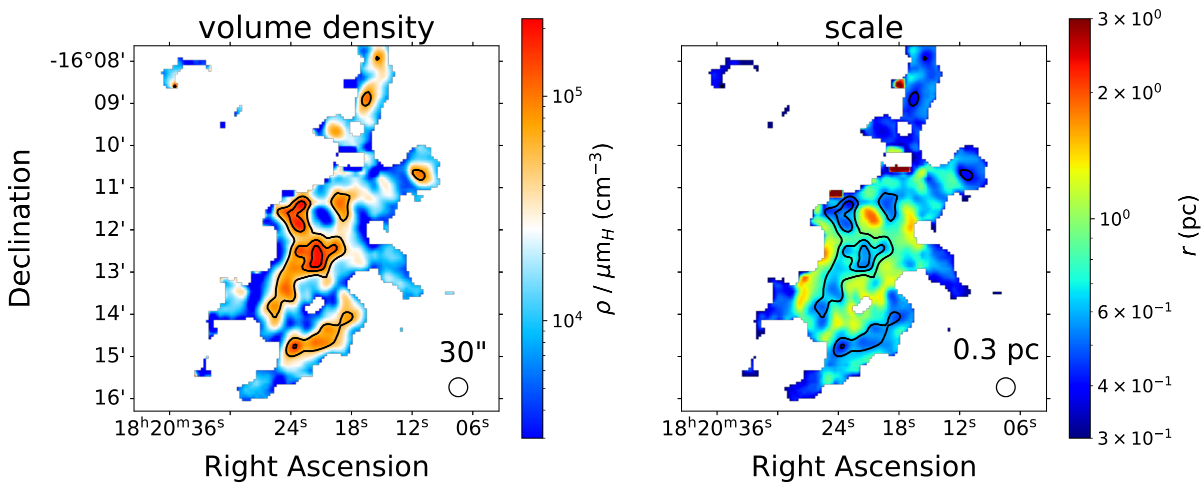

Figure 12. Decompose the column density as volume density and characteristic scale map.

Appendix C
Physical Parameters for Estimating Magnetic Field Strength

In this work, the physical parameter for measuring the magnetic field strength only utilizes two datasets to minimize systematic errors from observation: the observation of 850 μm dust polarization and NH_3 (1–1) (2–2). The H_2 volume density is obtained by decomposing the column density using MDR (details shown in Appendix B; M. Zhao et al. 2026), where the column density comes from 850 μm continuum emission and the gas temperature from NH_3. The volume density, nonthermal velocity dispersion, and magnetic field orientation angle dispersion are the necessary parameters to estimate magnetic field by turbulence–magnetic energy equipartition (L. Davis 1951; S. Chandrasekhar & E. Fermi 1953; R. M. Crutcher et al. 2004; J. Liu et al. 2021; R. Skalidis & K. Tassis 2021; R. Skalidis et al. 2021). The details of distribution are shown in Figure 13.

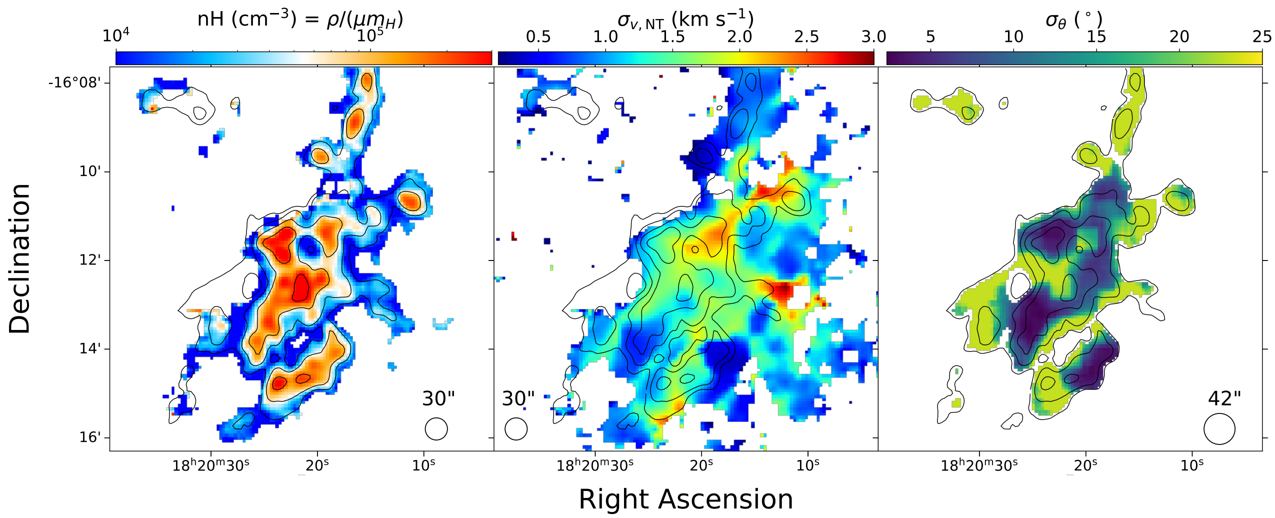

Figure 13. Distribution of volume density, nonthermal velocity dispersion, and magnetic field orientation angle dispersion.

Appendix D
Comparison of ST and DCF Methods

While the main text utilizes the ST (R. Skalidis & K. Tassis 2021; R. Skalidis et al. 2021) method due to its consideration of compressible turbulence modes, the DCF (L. Davis 1951; S. Chandrasekhar & E. Fermi 1953; J. Liu et al. 2022) method remains a standard benchmark in the field. To ensure our conclusions regarding the energy budget are model independent, we compare the results of both techniques.

The DCF field strength is calculated as

$$B_{\text{pos, DCF}} = Q\sqrt{4\pi\rho}\,\frac{\sigma_v}{\sigma_\theta}, \tag{D1}$$

where we adopt a correction factor of $Q = 0.4$ (J. Liu et al. 2021). Figure 14 presents the comparison. The ST method yields a mean POS magnetic field strength of $B_{\text{pos,ST}} = 0.54^{+1.9}_{-0.4}$ mG, while the DCF method yields $B_{\text{pos,DCF}} = 0.7^{+4.6}_{-0.6}$ mG. The systematic difference is approximately 25%, which is within the typical uncertainty range for polarization-based estimates.

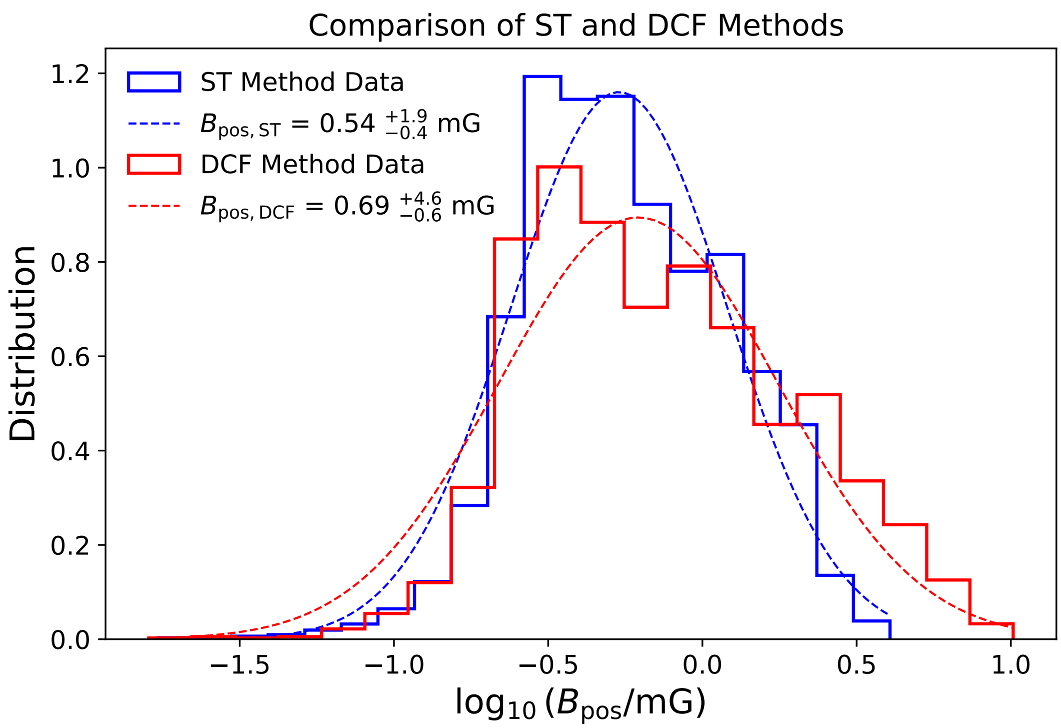

Figure 14. Comparison of POS magnetic field strength estimates using the ST and DCF methods. Histograms of the POS magnetic field strength (B_{pos}) derived from the ST method (blue) and the DCF method (red). The red dashed lines show the Gaussian fits. The ST method yields a mean of ∼0.54 mG, while DCF yields ∼0.69 mG.

Appendix E
Uncertainties in Gravitational Potential from Geometric Assumptions

We estimated the gravitational potential assuming a flattened slab geometry with a fixed effective half-thickness (Equation 2) in Section 3.2. To quantify the uncertainties introduced by this simplified geometric assumption, we tested the sensitivity of the derived gravitational energy density (e_G) to the assumed LOS extent of the cloud. We varied the total effective cloud thickness across a broad parameter space, ranging from 0.6 to 3.6 pc.

Figure 15 presents the resulting pdfs of e_G for these varying geometric scenarios. A larger assumed thickness naturally distributes the observed column density over a longer sightline, thereby diluting the local volume density. This dilution slightly reduces the absolute magnitude of the gravitational potential and its corresponding energy density. Consequently, the mean value of the gravitational energy density ($\langle \log e_G \rangle$) shifts gradually from -7.69 to -8.07 as the cloud thickness increases from 0.6 to 3.6 pc.

Despite this anticipated geometric variance, the gravitational energy density consistently governs the energy budget. Across all tested spatial configurations, $\langle \log e_G \rangle$ remains strictly higher than both the mean magnetic energy density ($\langle \log e_B \rangle = -8.25$) and the turbulent kinetic energy density ($\langle \log e_k \rangle = -8.71$). This exploration confirms the primary dynamical conclusion. The characterization of M17 SW as a globally gravity-dominated system is remarkably robust, remaining entirely unaffected by uncertainties in the unconstrained LOS geometry.

Extracting the turbulent magnetic field in the ST and DCF methods requires spatial smoothing to filter out the large-scale ordered field (L. Davis 1951; S. Chandrasekhar & E. Fermi 1953; J. Liu et al. 2021, 2022). The resolution of the background order magnetic field should distinctly differ to observed beam size. We adopt a physical lower limit of 42″, corresponding to 3 times (half dex) 14″ beam size.

To assess the sensitivity of our results to this parameter, we recalculated the magnetic field strength using smoothing kernels of 42″, 56″, and 70″ (representing 3×, 4×, and 5× the beam size). Figure 16 presents the resulting distributions. Increasing the kernel size from 42″ to 56″ slightly reduces the mean B_{pos} from 0.54 to 0.39 mG, after which the value stabilizes.

This slight decrease in B_{pos} at larger smoothing scales perfectly aligns with fundamental physical expectations. A larger spatial kernel effectively averages the parameters over a broader physical extent, inherently incorporating a higher fraction of the lower-density envelope gas. According to the well-established magnetic field-density (B–ρ) relation, magnetic field strength intrinsically scales with gas density (R. M. Crutcher et al. 2010; H.-B. Li et al. 2015; M. Zhao et al. 2024c). Therefore, measuring a weaker mean B_{pos} at a larger, less-dense macroscopic scale is a direct physical manifestation of the cloud's hierarchical structure, rather than a methodological artifact.

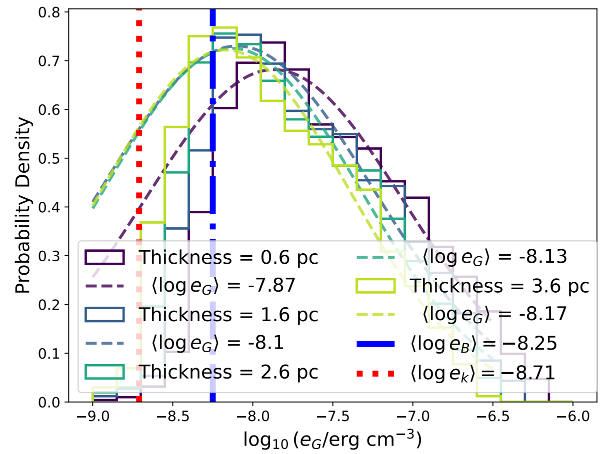

Figure 15. Probability density distributions of the gravitational energy density (e_G) under varying assumptions for the line-of-sight cloud thickness. The simulated effective thicknesses range from 0.6 to 3.6 pc. Dashed curves represent Gaussian fits to each distribution, with their respective mean values ($\langle \log e_G \rangle$) annotated in the legend. For direct comparison, the mean magnetic energy density ($\langle \log e_B \rangle = -8.25$) and turbulent kinetic energy density ($\langle \log e_k \rangle = -8.71$) are denoted by the blue dashed–dotted and red dotted vertical lines. The gravitational energy density unequivocally remains the dominant component across all tested geometric configurations.

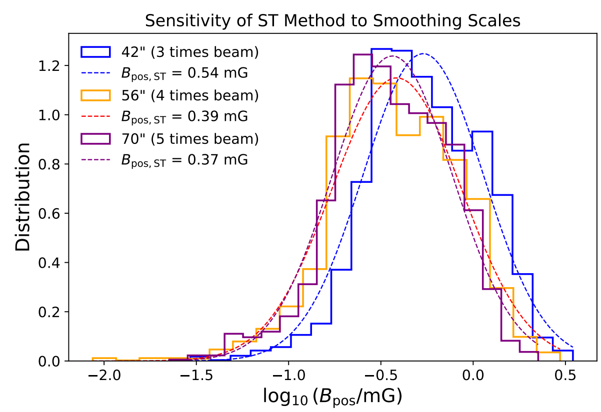

Figure 16. Probability density distributions of the plane-of-sky magnetic field strength (B_{pos}) derived using the ST method with varying spatial smoothing kernels: 42″ (blue), 56″ (orange), and 70″ (purple). The dashed curves represent Gaussian fits, with the mean field strengths annotated. The inferred field strength slightly decreases and stabilizes at larger smoothing scales, which further reinforces the gravity-dominated dynamical state of the cloud.

ORCID iDs

Mengke Zhao https://orcid.org/0000-0003-0596-6608
Keping Qiu https://orcid.org/0000-0002-5093-5088
Ji-hyun Kang https://orcid.org/0000-0001-7379-6263
Xindi Tang https://orcid.org/0000-0002-4154-4309
Anthony Whitworth https://orcid.org/0000-0002-1178-5486
Derek Ward-Thompson https://orcid.org/0000-0003-1140-2761
Takashi Onaka https://orcid.org/0000-0002-8234-6747
Chang Won Lee https://orcid.org/0000-0002-3179-6334
Tyler L. Bourke https://orcid.org/0000-0001-7491-0048
Jihye Hwang https://orcid.org/0000-0001-7866-2686
David Eden https://orcid.org/0000-0002-5881-3229
Thiem Hoang https://orcid.org/0000-0003-2017-0982
Motohide Tamura https://orcid.org/0000-0002-6510-0681
Jungmi Kwon https://orcid.org/0000-0003-2815-7774
Felix Priestley https://orcid.org/0000-0002-5858-6265
Kee-Tae Kim https://orcid.org/0000-0003-2412-7092
Doris Arzoumanian https://orcid.org/0000-0002-1959-7201
James Di Francesco https://orcid.org/0000-0002-9289-2450
Chakali Eswaraiah https://orcid.org/0000-0003-4761-6139
Doug Johnstone https://orcid.org/0000-0002-6773-459X
Bich Ngoc Nguyen https://orcid.org/0000-0002-5913-5554
Zhiwei Chen https://orcid.org/0000-0003-0849-0692
Sarah Sadavoy https://orcid.org/0000-0001-7474-6874
Archana Soam https://orcid.org/0000-0002-6386-2906
Ray S. Furuya https://orcid.org/0000-0003-0646-8782
Shih-Ping Lai https://orcid.org/0000-0001-5522-486X
Woojin Kwon https://orcid.org/0000-0003-4022-4132
Pierre Bastien https://orcid.org/0000-0002-0794-3859
Kate Pattle https://orcid.org/0000-0002-8557-3582
David Berry https://orcid.org/0000-0001-6524-2447

References

Bastien, P. 2020, in Stellar Magnetism: A Workshop in Honour of the Career and Contributions of John D. Landstreet, 11, ed. G. Wade et al., 117
Benjamin, R. A., Churchwell, E., Babler, B. L., et al. 2003, PASP, 115, 953
Berry, D. S., Gledhill, T. M., Greaves, J. S., & Jenness, T. 2005, ASPC, 343, 71
Brogan, C. L., Troland, T. H., Roberts, D. A., & Crutcher, R. M. 1999, ApJ, 515, 304
Cao, Z., & Li, H.-b. 2023, ApJL, 946, L46
Carey, S. J., Noriega-Crespo, A., Mizuno, D. R., et al. 2009, PASP, 121, 76
Chandrasekhar, S., & Fermi, E. 1953, ApJ, 118, 113
Chapin, E. L., Berry, D. S., Gibb, A. G., et al. 2013, MNRAS, 430, 2545
Chen, Z., Jiang, Z., Wang, Y., et al. 2012, PASJ, 64, 110
Chen, Z., Johnstone, D., Contreras Peña, C., et al. 2025, AJ, 170, 125
Crutcher, R. M. 2012, ARA&A, 50, 29
Crutcher, R. M., Nutter, D. J., Ward-Thompson, D., & Kirk, J. M. 2004, ApJ, 600, 279
Crutcher, R. M., Wandelt, B., Heiles, C., Falgarone, E., & Troland, T. H. 2010, ApJ, 725, 466
Davis, L. 1951, PhRv, 81, 890
Dempsey, J. T., Friberg, P., Jenness, T., et al. 2013, MNRAS, 430, 2534
Friesen, R. K., Pineda, J. E., Rosolowsky, E., et al. 2017, ApJ, 843, 63
Hanson, M. M., Howarth, I. D., & Conti, P. S. 1997, ApJ, 489, 698
Haworth, T. J., Tasker, E. J., Fukui, Y., et al. 2015, MNRAS, 450, 10
He, Z.-Z., Li, G.-X., & Burkert, A. 2023, MNRAS, 526, L20
Hoang, T. D., Ngoc, N. B., Diep, P. N., et al. 2022, ApJ, 929, 27
Hu, Y., Lazarian, A., & Stanimirović, S. 2021, ApJ, 912, 2
Hu, Y., Yuen, K. H., & Lazarian, A. 2019, ApJ, 886, 17
Keown, J., Di Francesco, J., Rosolowsky, E., et al. 2019, ApJ, 884, 4
Lada, C., Dickinson, D. F., & Penfield, H. 1974, ApJL, 189, L35
Lada, C. J., Depoy, D. L., Merrill, K. M., & Gatley, I. 1991, ApJ, 374, 533
Larson, R. B. 1981, MNRAS, 194, 809
Li, G.-X. 2022, ApJS, 259, 59
Li, G.-X., & Burkert, A. 2018, MNRAS, 474, 2167
Li, G.-X., & Zhou, J.-X. 2022, MNRAS, 514, L16
Li, H.-B. 2021, Galax, 9, 41
Li, H.-B., Yuen, K. H., Otto, F., et al. 2015, Natur., 520, 518
Li, S., Sanhueza, P., Beuther, H., et al. 2024, NatAs, 8, 472
Lim, W., De Buizer, J. M., & Radomski, J. T. 2020, ApJ, 888, 98
Liu, J., Qiu, K., & Zhang, Q. 2022, ApJ, 925, 30
Liu, J., Zhang, Q., Commerçon, B., et al. 2021, ApJ, 919, 79
Mairs, S., Dempsey, J. T., Bell, G. S., et al. 2021, AJ, 162, 191
Mathis, J. S., Rumpl, W., & Nordsieck, K. H. 1977, ApJ, 217, 425
McKee, C. F., & Ostriker, E. C. 2007, ARA&A, 45, 565
Ossenkopf, V., & Henning, T. 1994, A&A, 291, 943
Pattle, K., Fissel, L., Tahani, M., Liu, T., & Ntormousi, E. 2023, ASPC, 534, 193
Pattle, K., Ward-Thompson, D., Berry, D., et al. 2017, ApJ, 846, 122
Planck Collaboration, Aghanim, N., Akrami, Y., et al. 2020, AAP, 641, A12
Polychronakis, A., Tritsis, A., Skalidis, R., & Tassis, K. 2025, A&A, 700, A256
Povich, M. S., Churchwell, E., Bieging, J. H., et al. 2009, ApJ, 696, 1278
Priestley, F. D., & Whitworth, A. P. 2021, MNRAS, 506, 775
Qiu, K., Zhang, Q., Menten, K. M., et al. 2014, ApJL, 794, L18
Romeo, A. B., & Mogotsi, K. M. 2017, MNRAS, 469, 286
Romeo, A. B, & Mogotsi, K. M. 2018, MNRAS, 480, L23
Shu, F. H., Adams, F. C., & Lizano, S. 1987, ARA&A, 25, 23
Skalidis, R., Sternberg, J., Beattie, J. R., Pavlidou, V., & Tassis, K. 2021, A&A, 656, A118
Skalidis, R., & Tassis, K. 2021, A&A, 647, A186
Tritsis, A. 2026, A&A, 706, A60
Vázquez-Semadeni, E., Palau, A., Ballesteros-Paredes, J., Gómez, G. C., & Zamora-Avilés, M. 2019, MNRAS, 490, 3061
Ward-Thompson, D., Pattle, K., Bastien, P., et al. 2017, ApJ, 842, 66
Wilson, T. L., Hanson, M. M., & Muders, D. 2003, ApJ, 590, 895
Xu, Y., Moscadelli, L., Reid, M. J., et al. 2011, ApJ, 733, 25
Zhao, M., Li, G.-X., & Qiu, K. 2024a, ApJ, 976, 209
Zhao, M., Li, G.-X., & Qiu, K. 2024b, arXiv:2408.09690
Zhao, M., Li, G.-X., Xu, D., & Qiu, K. 2026, ApJ, 997, 345
Zhao, M., Zhou, J., Baan, W. A., et al. 2024c, ApJ, 967, 18
Zhao, M., Zhou, J., Hu, Y., et al. 2022, ApJ, 934, 45
Zhu, F.-Y., Wang, J., Yan, Y., Zhu, Q.-F., & Li, J. 2023, MNRAS, 522, 503